High Temperature Corrosion under Laboratory Conditions Simulating Biomass-Firing: A Comprehensive Characterization of Corrosion Products

Okoro, Sunday Chukwudi; Montgomery, Melanie; Jappe Frandsen, Flemming; Pantleon, Karen

Published in:
Energy and Fuels

Link to article, DOI:
10.1021/ef5017335

Publication date:
2014

Document Version
Peer reviewed version

High temperature corrosion under laboratory conditions simulating biomass firing: A comprehensive characterization of corrosion products

Sunday Chukwudi Okoro[1*], Melanie Montgomery[1,3], Flemming Jappe Frandsen[2], Karen Pantleon[1]

[1]Technical University of Denmark (DTU), Department of Mechanical Engineering, 2800 Kongens Lyngby, Denmark.

[2]DTU, CHEC Research Centre, Department of Chemical and Biochemical Engineering, 2800 Kongens Lyngby, Denmark.

[3]COWI A/S, Parallelvej 2, 2800 Kongens Lyngby, Denmark

Abstract

An austenitic stainless steel (TP 347H FG) was coated with a synthetic deposit and exposed, under laboratory conditions simulating straw-firing at 560 °C, for one week. Microscopic, diffraction and spectroscopic techniques were employed for cross-sectional and plan view 'top-down' microstructural characterization of the corrosion products. The corrosion products consisted of three layers: i) the outermost layer consisting of a mixed layer of K_2SO_4 and Fe_xO_y on a partly molten layer of the initial deposit, ii) the middle layer consists of spinel ($FeCr_2O_4$) and Fe_2O_3, and iii) the innermost layer is a sponge-like Ni_3S_2 containing layer. At the corrosion front, Cl-rich protrusions were observed. Results indicate that selective corrosion of Fe and Cr by Cl, active oxidation and sulphidation attack of Ni are possible corrosion mechanisms.

Keywords: Stainless steel, Biomass, High temperature corrosion, Chlorination, Sulphidation.

1. Introduction

The increasing CO_2-levels in the atmosphere have necessitated the use of renewable energy sources such as biomass, for 'CO_2 neutral' heat and power production. Power plants in Denmark are currently firing biomass (straw and wood) as a substitute for fossil fuels, mainly coal. Biomass is considered CO_2 neutral since it recaptures the CO_2 released during combustion through photosynthesis within a short period of time (~10^0 years), compared to the time for coal seam formation (~10^6 years). Furthermore, the widespread availability of biomass makes its utilization for heat and power production a viable energy source. Despite these encouraging attributes, the chemistry of biomass is quite different from that of fossil fuels [1–3]. Fuels with a high content of K and Cl are usually labelled troublesome since they form low-melting, sticky deposits leading to slagging and fouling problems. Moreover Cl plays a vital role in the catastrophic corrosion observed in heat exchangers (superheaters) in biomass-fired boilers, especially those utilizing straw [4,5].

Since biomass contains significant amounts of flame-volatile alkali metal salts [6–9], the ash deposit challenges from combustion of these fuels differ considerably from fossil fuels. Through diffusion, thermophoresis, condensation or inertial impaction, gaseous alkali species, alkali-rich aerosols and fly ash particles are able to form thick deposits on cooler parts of the heat exchangers, where heat is transferred from the hot flue gas into the steam cycle [10–13]. These aerosol particles consist mainly of potassium chloride (KCl) and potassium sulphate (K_2SO_4) [14,15], which are two species known to cause significant operational challenges due to fouling and corrosion of heat exchangers [16].

To lessen the corrosion of superheater components, the outlet temperature of the final superheater is kept relatively low, i.e. at or below approximately 540 ˚C in Denmark. This result in a lower efficiency of the power plants compared to coal-firing plants. Thus, there is a strong need for alternative solutions to corrosion problems in order for biomass to remain an economically viable energy source. This task is anchored on comprehending fully the mechanisms involved in the corrosion process. This will guide the development of alloyed materials which can be utilized as superheaters in boilers firing biomass.

Full-scale corrosion tests have been carried out in power plants in order to ascertain corrosion rates and mechanisms. Generally, the high corrosion rate observed during straw-firing is attributed to the following active oxidation mechanism caused by Cl [17–19]. Sulphation of the condensed KCl close to the superheater tubes generates Cl. This penetrates the initial oxide layer and reacts with the alloying elements giving rise to metal chlorides. At the oxide/alloy interface, these metal chlorides possess high vapor pressures and hence vaporize to the oxide/gas interface, where they become oxidized due to sufficient oxygen partial pressures at these locations [13,20]. Part of the Cl liberated from this oxidation is able to diffuse back to the corrosion front where it reacts again with the alloy, thereby propagating the corrosion process. However, the unavoidable variations in operating temperatures and fuel type tend to complicate the assessment and thus hinder full understanding of this mechanism. As a result, laboratory-scale studies are employed to study corrosion under well-controlled (although often greatly simplified) conditions with a focus on specific parameters. Simplified laboratory-scale corrosion studies using synthetic deposits (KCl, NaCl, $CaCl_2$, etc.), and in some cases, under HCl- or H_2O-containing gaseous atmospheres, have revealed the respective roles of K and Cl in initiating and catalyzing the corrosion of alloys under oxidizing conditions [4,5,21–30]. The results from characterization of corrosion products from most of these laboratory studies point towards an active oxidation type of mechanism. However, few studies [13,31–33] have investigated both the influence of the flue gas and the synthetic deposit in order to discover more information regarding the corrosion mechanisms under such realistic, but complex conditions. Comprehensive characterization is difficult with standard metallographic techniques due to the heterogeneous nature of corrosion products from such studies and the fact that many of the chloride containing products are water soluble.

The mechanistic conclusions from both full-scale and laboratory-scale studies are often based on Light Optical Microscopy (LOM), Scanning Electron Microscopy (SEM) and chemical elemental analysis (by Energy Dispersive Spectroscopy - EDS), on metallographically prepared sample cross sections [31,32], or on plan view of exposed samples [5,22]. A weakness of this approach, is that localized and sub-surface features arising from the corrosion process tend to be obscured if they are absent along the examined cross section, or if they are localized in a few microns area, and thus important information which could aid understanding is lost. Consequently, it is desirable to optimize the approach towards characterization of the corrosion products through a combination of cross-sectional, and a plan view 'top-down' technique. For combining site-specific local analysis with an increased area/volume of the investigated sample part, supplementary X-ray diffraction (XRD) analysis provides an additional advantage. Furthermore, XRD will enable a thorough phase analysis of crystalline corrosion products and thus complement the elemental analysis by EDS.

This paper reports on the application of both cross-sectional and a plan view 'top-down' complementary characterization methods for systematic analysis of high temperature corrosion of an austenitic stainless steel (TP 347H FG) after laboratory exposure to straw-firing gaseous conditions under a synthetic deposit in the laboratory. Corrosion products were investigated as a function of distance from the original deposit surface, based on both cross section and plan view analysis, combined with stepwise removal of the corrosion products. The complementary information obtained from microscopy (by LOM and SEM), elemental analysis (by EDS) and qualitative phase analysis (by XRD), allowed the depth-resolved characterization of corrosion products. This comprehensive characterization helped to effectively discuss the corrosion mechanisms under the exposure conditions.

2 Experimental

2.1 Sample preparation and high temperature exposure

A fine grained (FG) austenitic stainless steel (TP 347H FG) tube with the composition shown in Table 1 was investigated. The tube was sectioned into rings of width 1 cm. From these rings, arc shaped specimens with an average internal surface area of 1.2 cm^2 were cut. These tube pieces were degreased in acetone and then ethanol, in an ultrasonic bath prior to synthetic deposit coating.

Table 1. EDS measured chemical composition (in wt.%), of the as-received austenitic stainless steel (TP 347H FG) investigated

Si	Cr	Mn	Ni	Fe	Nb

0.4	18.1	2.0	10.3	68.7	0.5

The concave side of the curved tube pieces was covered with a synthetic deposit of pure KCl (Sigma, ≥ 99%). For this purpose, a deposit slurry was prepared by mixing 32 – 60 µm sized KCl particles with 2-propanol. The slurry was applied such that, after solvent evaporation, a uniform coating of about 52.1 mg cm^{-2} of the deposit was obtained on the surface. The use of deposit slurries is in accordance with the EU guidelines [34,35] for hot corrosion testing, and also enhances effective simulation of high temperature corrosion under alkali chloride deposits as observed in power plants.

High temperature exposure of the coated specimen was carried out in a corrosion test rig [13,33] consisting of an electrically heated horizontal furnace, a gas mixing panel and a flue gas clean-up system. A schematic sketch of the corrosion test-rig is shown in Fig. 1. The test-rig contains five quartz tubes which allow five exposures under a similar gas environment (in the present work, only one distinct exposure condition is considered). Mass flow controllers were employed to regulate the concentration of the respective gases making up the simulated flue gas.

Table 2 presents the gas composition employed to simulate the flue gas composition during straw-firing, as measured in a Danish power plant firing straw [32]. The concentration of HCl used is a worst case level as the average concentration in straw-firing is approximately 70 ppm. To ensure a uniform gas flow rate in each reactor, ball flow meters were also connected at the exit of each reactor. The KCl coated specimens were exposed at 560 ^{o}C for 168 hours in the corrosion test-rig.

Additionally, in a separate experiment to investigate the possibility of K_2CrO_4 sulphation under the simulated straw-firing condition, as-received K_2CrO_4 particles were exposed to the same flue gas composition used to simulate straw-firing at 560 ^{o}C for 168 h.

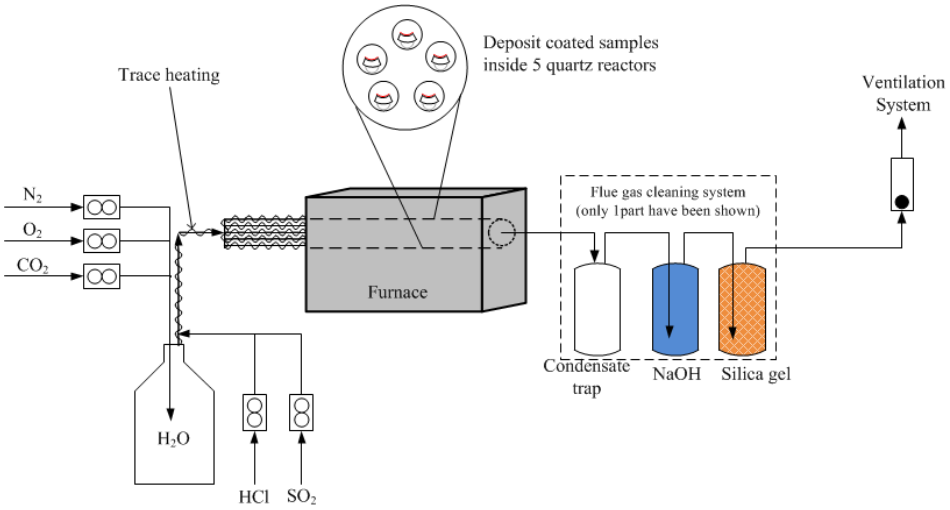

Figure 1. Schematic illustration of the corrosion test rig employed for the high-temperature exposure. The electrically heated horizontal furnace contains 5 quartz reactors, which allows for 5 simultaneous experiments under similar flue gas conditions. Only 1 (out of the 5) flue gas cleaning systems have been shown.

Table 2. Composition of the (dry) flue gas employed to simulate straw firing conditions

Gas	Concentration in flow
N_2	82 vol.-% (dry)
O_2	6 vol.-% (dry)
CO_2	12 vol.-% (dry)
SO_2	60 ppmv (dry)
HCl	400 ppmv (dry)

2.2 Characterization of exposed samples

After cooling to room temperature, the exposed samples were investigated by microscopic (LOM, SEM), and diffraction based (XRD) techniques, in addition to chemical compositional analysis (EDS). The comprehensive characterization of the exposed samples involved both a cross-sectional approach and a plan view 'top-down' approach through removal of corrosion products.

For cross-sectional investigation, an exposed sample was first mounted in epoxy under vacuum, which ensured a rather tight embedding and preserved the sample morphology. The embedded sample was further sectioned along its length-axis, and subsequently re-embedded with the cut surface facing downwards in order to access the sample's cross section. The final embedded sample was ground and polished according to standard metallographic sample preparation procedure, but under water-free conditions. As a substitute, absolute ethanol (VWR chemicals, 99.9 %) was utilized during grinding and polishing to preserve the water-soluble corrosion products.

Plan view 'top-down' analysis was carried out on exposed samples without any embedding. Microscopic, spectroscopic and diffraction based characterizations were first carried out directly on the surface of the exposed sample and then, combined with removal of various layers of the corrosion product. A schematic sketch showing the directions and locations from which the characterization stages were undertaken is shown in Fig. 2.

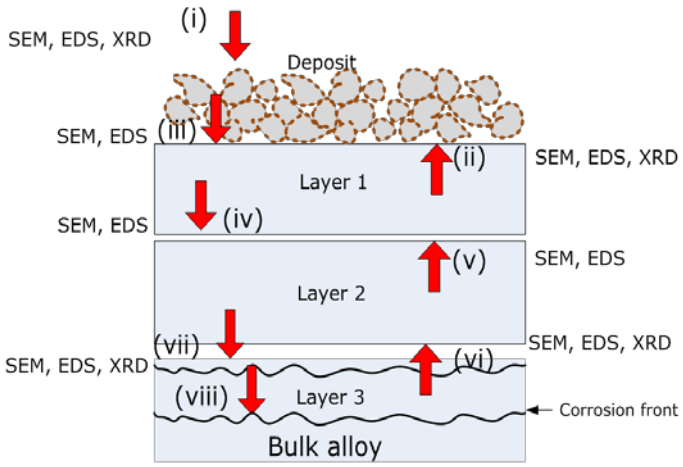

Figure 2. Schematic illustration of the depth-resolved top view characterization process. Arrows are used to show the direction from which the characterization was carried out. Employed characterization techniques at each point are also shown.

A scalpel and at larger depths, SiC paper were used to remove the synthetic KCl deposit and the resulting corrosion products. In cases where large deposits and corrosion product layers could be removed as compact pieces, the underside of these was also investigated. This removal is a dry process which does not involve solvents of any kind. The weight difference after each removal step was monitored for estimating the removed layer thickness assuming a homogenous layer distribution. A related approach had earlier been employed for XRD stress analysis of oxide phases on the steam side of superheater tubes [36].

The reaction product resulting from the additional separate exposure of K_2CrO_4 to straw-firing conditions was characterized by SEM, EDS and XRD.

2.3 Characterization techniques

Cross-sections of the exposed samples were examined by means of LOM (OLYMPUS GX 41) to investigate the microstructure, thickness and morphology of the various corrosion products. The metallographically prepared samples were etched by swabbing with glyceregia for ca. 6 sec and afterwards rinsed with deionized water before LOM investigations.

SEM was employed for both cross section and plan view characterization of the exposed samples. Both secondary electron (SE) and backscattered electron (BSE) images were used to obtain information on the morphology and chemical composition of the corrosion products. A SEM (FEI, Inspect S and JEOL, JSM 5900) operated with an acceleration voltage of 15 keV was used.

Elemental analysis of corrosion products was carried out, both on cross sections and as plan view measurements, applying an Oxford Inca EDS system. The EDS system was connected to the SEM, which was also operated with an acceleration voltage of 15 keV during EDS-analysis.

X-ray diffraction was carried out on the concave sample surface, both directly after exposure and after the various removals of the corrosion products. XRD was carried out using a diffractometer (D8 Discover) from Bruker AXS operated in grazing incidence geometry, with a point focused incident X-ray beam using a polycap optics system to converge the beam. The investigations were undertaken such that the sample length-axis (i.e. the longitudinal axis of the tube) with uniform sample height becomes parallel to the diffraction plan and thus eliminates the possibility of shielding the X-Ray beams. Measurements after the various layer removals were carried out with an X-ray incidence angle of 3 °, giving a constant penetration depth less than 1.3 µm within the range of measured diffraction angles (2θ = 30 – 135 °) for the applied Cr-Kα radiation. Measurements directly on the as-exposed sample surface, i.e. before any layer removal, were performed with an incidence angle of 5 °. However the penetration depth cannot be determined accurately due to the unknown absorption characteristics of the porous salt deposit. The sketch in Fig. 2 shows the different locations at which XRD investigations were carried out. For XRD measurements on the reaction products from the exposure of K_2CrO_4, the conventional Bragg-Brentano diffraction geometry was used with Cr-Kα radiation.

3. Results

3.1 Characterization across the cross section of the exposed sample

The microstructure of the sample cross section (cs), as observed with SEM using a BSE detector, is shown in Fig. 3a. From the micrograph, three layers of corrosion products (layer 1-cs to layer 3-cs) can be identified and magnified views of these different layers are presented in Figs. 3b and 3c. The thickness of these corrosion product layers is inhomogeneous. However, results from thickness measurements from 30 locations across the exposed sample cross section, showed the average thickness to be 31.3 ± 6.8 µm, 18.5 ± 7.8 µm and 10.8 ± 2.6 µm for layer 1-cs, layer 2-cs and layer 3-cs, respectively. To supplement microscopic analysis, EDS elemental mapping was also carried out (Fig. 4), to show the distribution of alloying elements or deposit/flue gas constituents within the corrosion product.

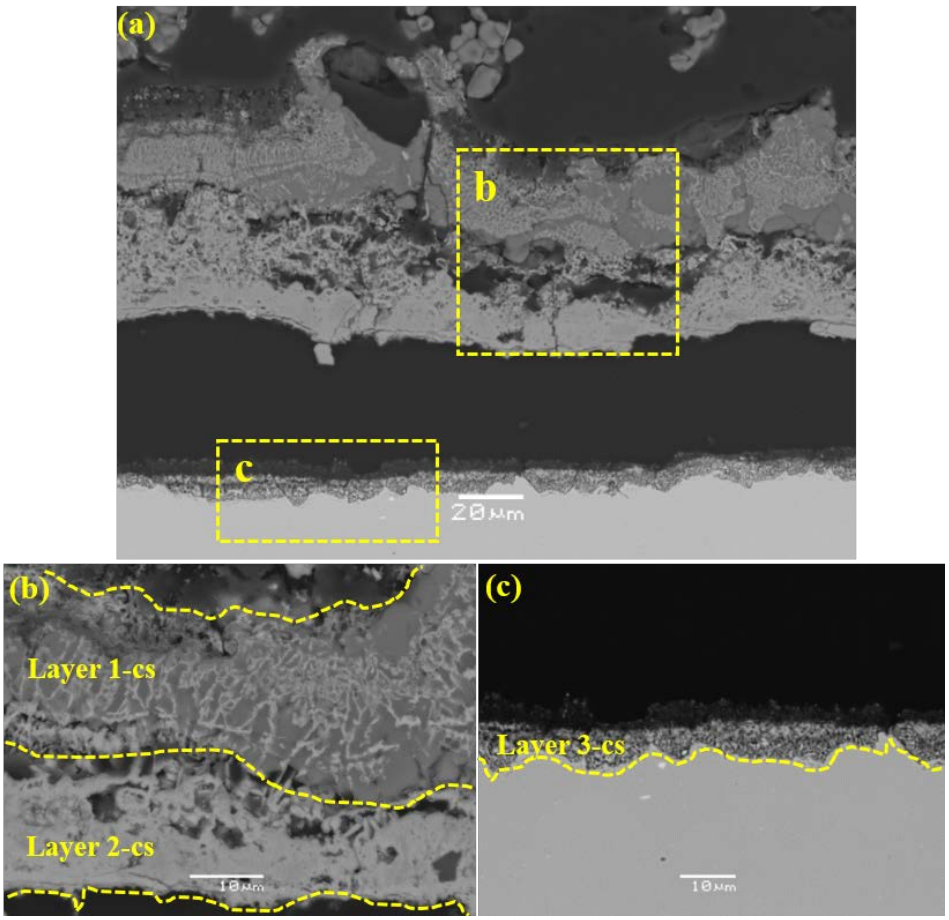

Figure 3. (a) Backscattered electron (BSE) micrograph of the exposed sample cross section. (b) shows a magnified view of the first two layers (layer 1-cs and 2-cs), (c) is a magnified view of the sponge-like layer (layer 3-cs).

The chemical composition of the three distinct layers of the corrosion products, which were identified by microscopy (Fig. 3), can be visualized in the EDS maps (Fig. 4). From the EDS maps, layer 1-cs consist of a mixed layer as already indicated by the contrast in the micrograph (see Fig. 3) and contains mainly K, Fe, S and O. A discontinuous band of Cl is observed above layer 1-cs. Layer 2-cs is revealed to consist of Fe, Mn, Cr, and O (see Fig. 4). This layer contains severe cracks as well as several voids, i.e. the layer possesses high porosity. Close to the bulk alloy, the sponge-like layer (layer 3-cs) is observed from the EDS maps to consist of Ni and S. This sponge-like layer is non-uniform and exhibits an irregular interface with the bulk of the alloy (Fig. 3c).

Upon etching the sample cross section with glyceregia, the microstructure of the steel below layer 3-cs was revealed as shown in Fig. 5. Selective attack along the grain boundaries is observed close to the corrosion front and is marked in the micrograph.

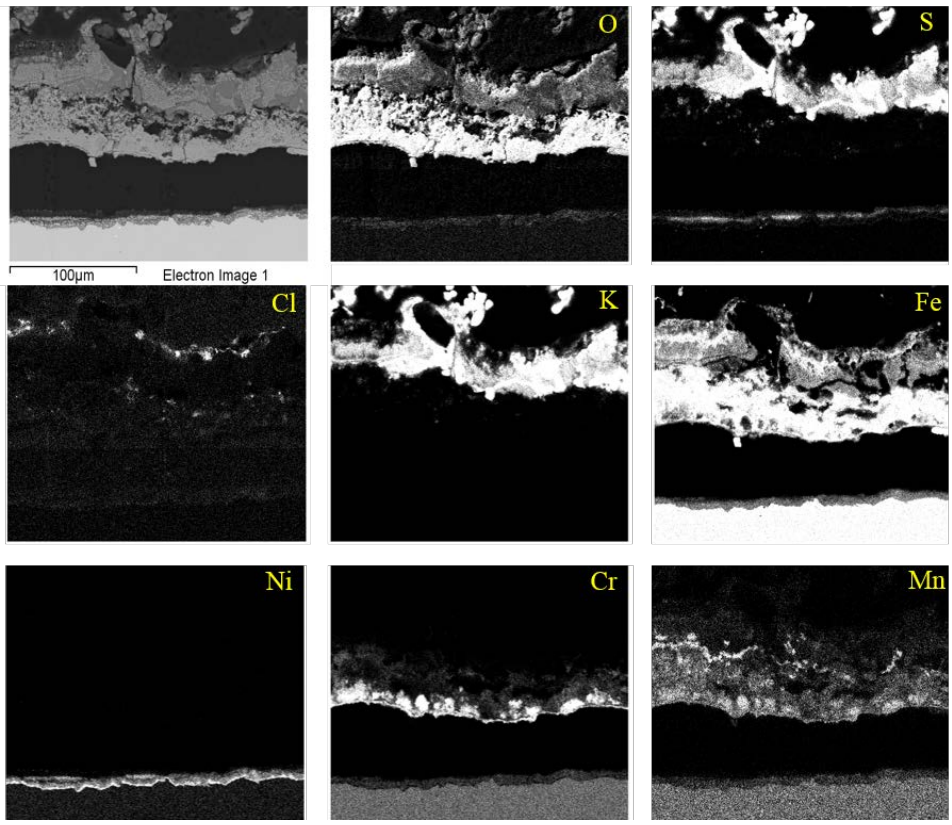

Figure 4. SEM image (upper left) and EDS elemental maps showing the chemical composition of the corrosion products across the cross section of the exposed sample.

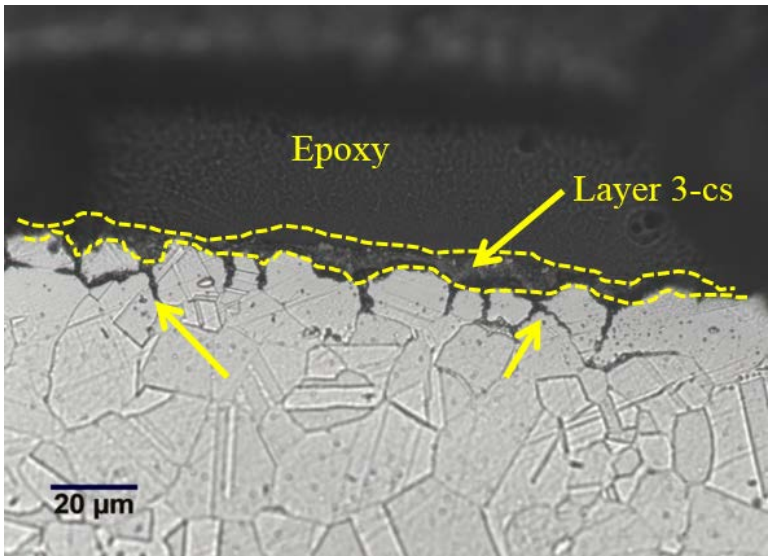

Figure 5. LOM micrograph showing the microstructure of the exposed sample cross section below the corrosion products after etching with glyceregia. Grain boundary attack is marked.

It is pertinent to mention that these corrosion product layers shown in the micrographs (Figs. 3 and 4) are observed directly below the initial (KCl) deposit. The embedding of the sample in epoxy to preserve the morphology of the corrosion products for cross-sectional examination obscures some information about the chemistry and morphology of the deposit after high temperature exposure. This is a result of interference from the embedding matrix during chemical elemental analysis, as well as the detachment of some of the deposit particles during metallographic preparation.

3.2 Depth-resolved characterization combined with successive layer removal

Plan view investigations by SEM (carried out at locations (i) and (ii) in Fig. 2) revealed the morphology of the synthetic deposit after exposure, as shown in Fig. 6. Small particle clusters are observed to accumulate around the initial KCl (deposit) particles. At the deposit/flue gas interface (Fig. 6a), the small particle clusters appear to have totally coated the initial deposit surface, while at the deposit/corrosion product interface (Fig. 6b) these particles appear as attachments to the initial deposit particles. EDS-analysis (see Table 3) on these particle clusters shows the presence of S in addition to K and Cl, thus, suggesting the sulphation of the initial synthetic deposit. The measured concentrations of K, S and O from EDS-analysis indicate the formation of K_2SO_4.

The diffractograms in Fig. 7 were recorded by XRD on the exposed sample, both at the deposit/flue gas interface and at the deposit/corrosion product interface (points (i) and (ii) in Fig. 2). Apart from KCl, K_2SO_4 can be identified on both measured sites (according to Joint Committee Powder Diffraction Standard (JCPDS) cards; 41-1476 and 83-681 for KCl and K_2SO_4 respectively).

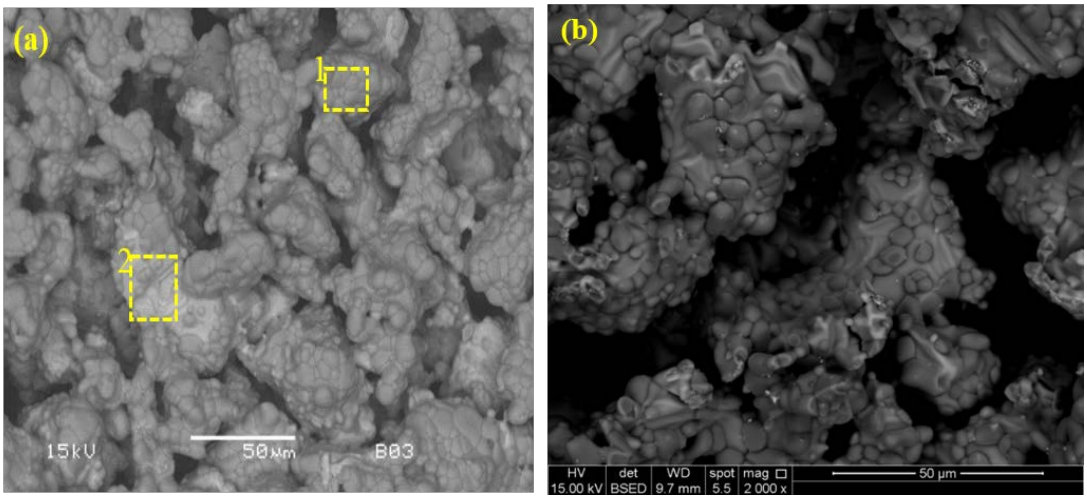

Figure 6. BSE micrographs showing the deposit particles, after high temperature exposure viewed both from (a): the flue gas/deposit interface and (b): the deposit/oxide layer interface (corresponding to locations (i) and (ii) in Fig. 2). Results from EDS-analysis on the selected regions are presented in Table 3.

Table 3. Elemental composition of selected regions at the flue gas/deposit interface (see Fig. 6a), determined by EDS-analysis

Region	Element (wt.-%)			
	O	S	Cl	K
1	38.2	18.6	0.4	42.9
2	18.7	7.0	31.0	43.3

XRD phase identification thus supports the EDS-data with respect to the sulphation of the initial deposit to yield K_2SO_4 (see results in Table 3). However, the additional detection of KCl by XRD (in conjunction with identification of K and Cl by EDS) also suggests incomplete sulphation of the deposit particles during exposure.

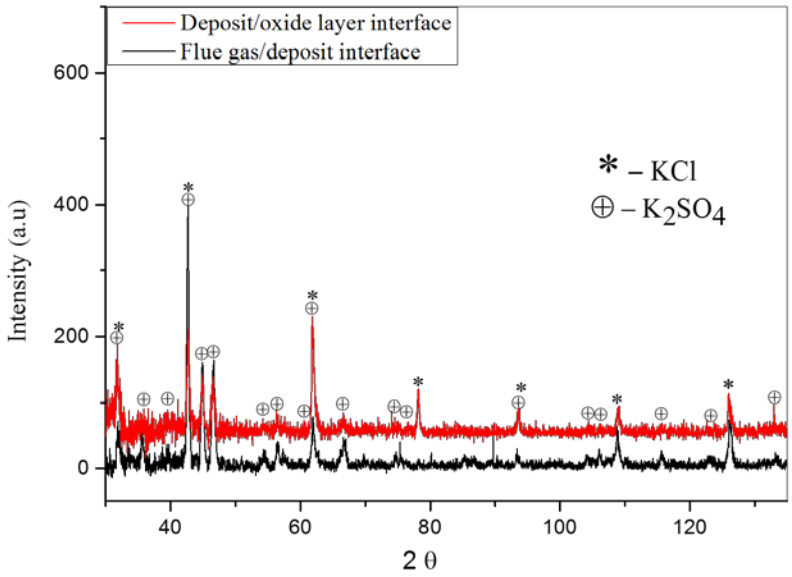

Figure 7. XRD phase analysis on the synthetic deposit, both at the flue gas/deposit interface and at the deposit/corrosion product interface, (i.e. points (i) and (ii) in Fig. 2).

Similar to the observation of distinct layers in the cross section analysis (-cs layers), also the plan view analysis revealed that the corrosion product consists of several layers (-pv layers). Two distinct layers of corrosion products were identified underneath the initial synthetic deposit. Fig. 8 shows the microstructures of these layers, as observed from the initial deposit/flue gas interface, and the interface between the first two layers of corrosion product (points (iii) and (iv) in Fig. 2). SE and BSE micrographs respectively reveal morphological and chemical contrast between these layers. An overview of both layer 1-pv and layer 2-pv is shown in Figs. 8a and 8b.

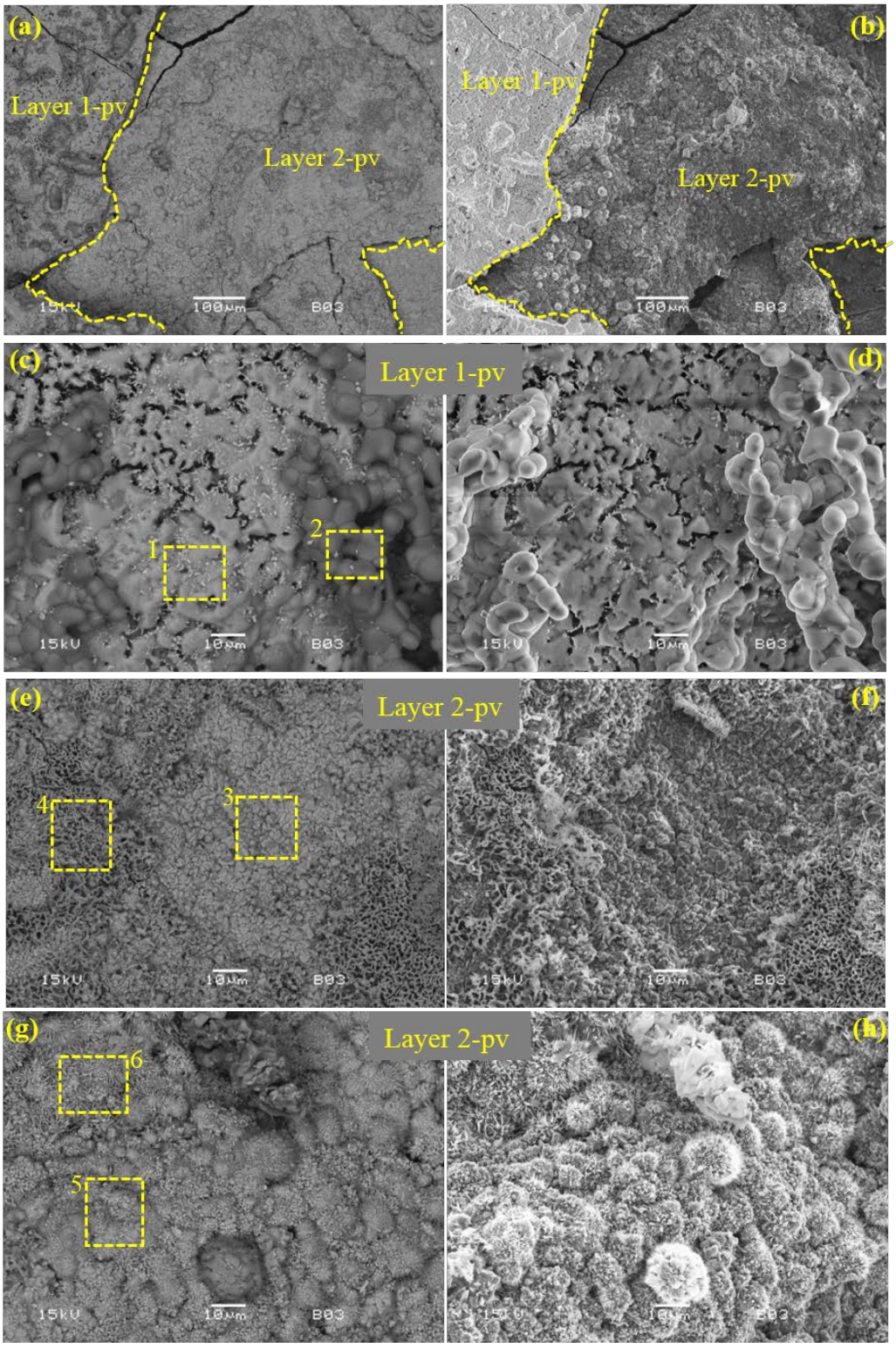

Figure 8. BSE (left column) and SE (right column) micrographs from plan view analysis showing layer 1-pv and layer 2-pv of the corrosion product (as viewed from the deposit/corrosion product interface –points (iii) and (iv) in Fig. 2), after the synthetic deposit has been removed. Results from

EDS-analysis on the marked regions are presented in Table 4. In (a) and (b), the two layers of corrosion products can be seen. Magnified BSE and SE images are shown for layer 1-pv in (c) and (d) and from different locations for layer 2-pv in (e)-(h).

Layer 1-pv (Figs. 8c-d) when viewed from point (iii) in Fig. 2, is observed to consist of isolated clusters of round-shaped particles lying on a continuous layer. The morphology of this continuous layer suggests that it has been partly molten. The continuous partly molten layer on layer 1-pv is also observed to contain embedded particle strands. Through EDS-analysis (see Table 4), the isolated clusters of round-shaped particles (region 2 in Fig. 8c) are found to be abundant in K, S and O. Conversely, on the partly molten continuous layer (region 1 in Fig. 8c), the major identified elements were K, Cl, O and Fe. Layer 1-pv (Figs. 8c-d) could correspond to layer 1-cs (cf. Fig. 3) which comprised of K, Fe, S and O, as observed from cross-sectional characterization of the exposed sample. From the plan view 'top-down' characterization method, it is observed that layer 1-cs could have been formed locally, rather than as a continuous layer as observed in the micrograph in Fig. 3. This highlights the need for complementing both characterization approaches for thorough characterization of corrosion products.

Table 4. Elemental composition of selected regions at the deposit/corrosion product interface (see Fig. 8), determined by EDS-analysis

Image	Region	Element (wt.-%)						
		O	S	Cl	K	Cr	Mn	Fe
Figure 8c	1	6.6	0.9	34.1	42.0	-	0.4	15.9
	2	34.0	18.7	0.5	44.7	-	-	2.0
Figure 8e	3	25.9	-	0.2	0.2	2.3	2.9	68.4
	4	26.6	-	1.2	1.3	15.2	1.3	54.4
Figure 8g	5	22.5	-	0.6	0.7	4.5	1.3	70.5
	6	22.2	-	4.3	3.9	2.2	0.5	66.9

The microstructure of layer 2-pv shown in Figs. 8e-h is more complex. SEM and EDS investigations on this layer were carried out from the direction indicated by point (iv) in Fig. 2. On some locations, faceted Fe-rich structures were observed (see Figs. 8e-f and Table 4). Surrounding these faceted structures, Fe-rich blade-like hollow structures containing appreciable amounts of Cr are also observed. These hollow shaped structures existed in a networked type of arrangement. Some faceted structures can also be identified within these structures. Other locations on layer 2-pv comprised of coral-like arrangement of particles (Figs. 8g-h). Whisker-like protuberances are observed within these coral-like arranged particles. EDS-analysis disclosed this layer to consist of O, Fe, Cr, K and Cl (see Table 4).

Fig. 9 presents the microstructure of the corrosion products beneath the synthetic deposit, but as viewed from the interface between layer 2 and layer 3. Directions from which the investigations were carried out are indicated as points (v) and (vi) in Fig. 2. Similar to the observation from Figs. 8a-b, two layers (layer 1-pv and layer 2-pv) of corrosion products are observed in the micrograph in Fig. 9a.

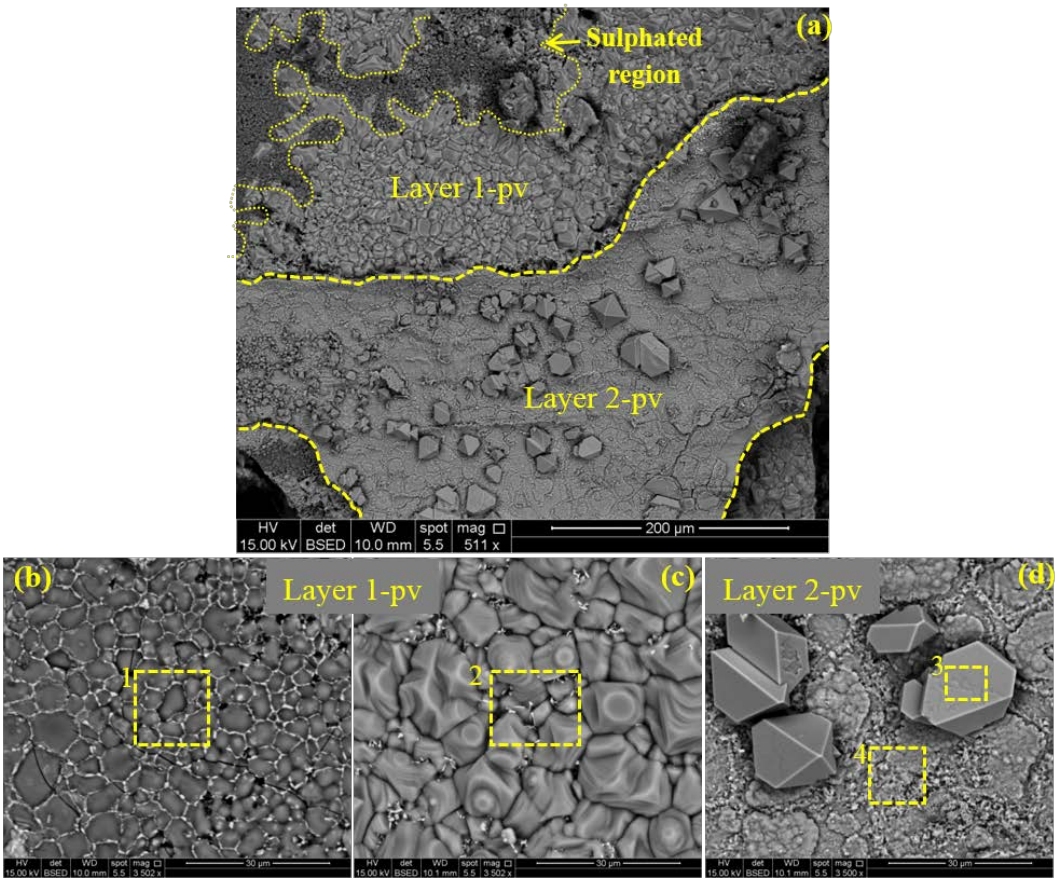

Figure 9. BSE micrographs showing the morphology of the corrosion products (as viewed from the interface between layers 2 and 3 of the corrosion product –indicated by points (v) and (vi) in Fig. 2), after the synthetic deposit has been removed. Two distinct layers of corrosion products are observed in (a) and magnified images are shown in (b)-(d). EDS results from selected regions on the micrographs are presented in Table 5.

The first layer (layer 1-pv) consists of segregated dark regions (Fig. 9b) amidst a brighter region having a partly molten and sintered morphology (Fig. 9c). This is similar to that observed in Fig. 8a-b. Within the segregated dark regions on layer 1-pv, bright particle strands are seen to accumulate around, and on the dark round-shaped particles. EDS-analysis showed the composition of this segregated dark regions to include O, S, K, and Fe, with minor amounts of Cl and Cr (see Table 5). The bright particle strands are similarly observed on the partly molten and sintered regions in layer 1-pv (Fig. 9c). The elemental composition of the partly molten and sintered region was determined by EDS-analysis to consist of Cl, K and O, with minor amounts of Cr and Fe

(Table 5). This observation reiterates the incomplete sulphation of the initial deposit particles under the exposure conditions. The second layer is observed to comprise of large facetted structures lying on a continuous layer (see Fig. 9d). The morphology of this layer shows non continuous regions in the form of platelets. The large facetted structures were identified by EDS-analysis (see Table 5) to contain O and Fe with a minor amount of Cr (1.6 wt.-%). On the continuous layer, O, Fe and high amounts of Cr (46 wt.-%) were identified by EDS-analysis. Minor amounts of Si, Ni, Mn, Nb, S, K and Cl were also identified on this layer in concentrations < 2 wt.-% (Table 5).

Table 5. Elemental composition of selected regions at the interface between corrosion product layers 1 and 2(see Fig. 9), determined by EDS-analysis

Image	Region	Element (wt.-%)									
		O	S	Cl	K	Cr	Mn	Fe	Si	Ni	Nb
Figure 9b	1	38.7	17.5	0.3	39.5	-	-	4.0	-	-	-
Figure 9c	2	3.2	-	46.2	45.7	0.8	-	4.1	-	-	-
Figure 9d	3	28.0	-	-	-	1.6	-	70.4	-	-	-
	4	22.6	-	0.9	0.5	46.4	1.0	25.1	0.8	0.4	1.9

XRD results from the interface between corrosion product layers 2 and 3 are shown in Fig. 10. XRD was carried out on the removed corrosion product from the direction indicated as point (vi) in Fig. 2. Phase identification is not straightforward for the present oxides, because slight variations of the chemical composition as well as the presence of macrostresses considerably cause deviations of the measured peak position compared to the theoretical data from the JCPDS for possible phases. However, in addition to K_2SO_4 and KCl (in agreement with Fig. 7), Fe_2O_3 (JCPDS card 33-664) and Cr-containing spinel (JCPDS card 34-140) were identified.

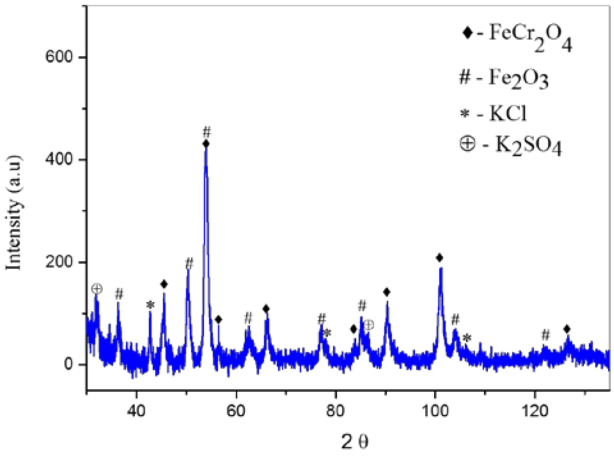

Figure 10. X-Ray diffractogram from the removed corrosion product beneath the synthetic deposit, i.e. from the interface between layers 2 and 3 of the corrosion product (point (vi) in Fig. 2).

The change in microstructure of the third layer of corrosion product (layer 3-pv), from the layer surface (L3S) towards the bulk of the alloy is shown in Fig. 11. Characterization of this layer was carried out from the direction indicated as point (vii) in Fig. 2.

A combination of the weight change after each removal step, and the density of the prevalent phases identified enabled an estimation of the thickness of the removed layer. EDS revealed high Ni and S concentrations (36.6 wt.-% Ni and 11.3 wt.-% S) on the surface of layer 3-pv (see region 2 in Table 6). Also in larger depth of 9.1 µm from L3S, EDS revealed (not shown here) that S is associated with Ni along the alloy grain boundaries.

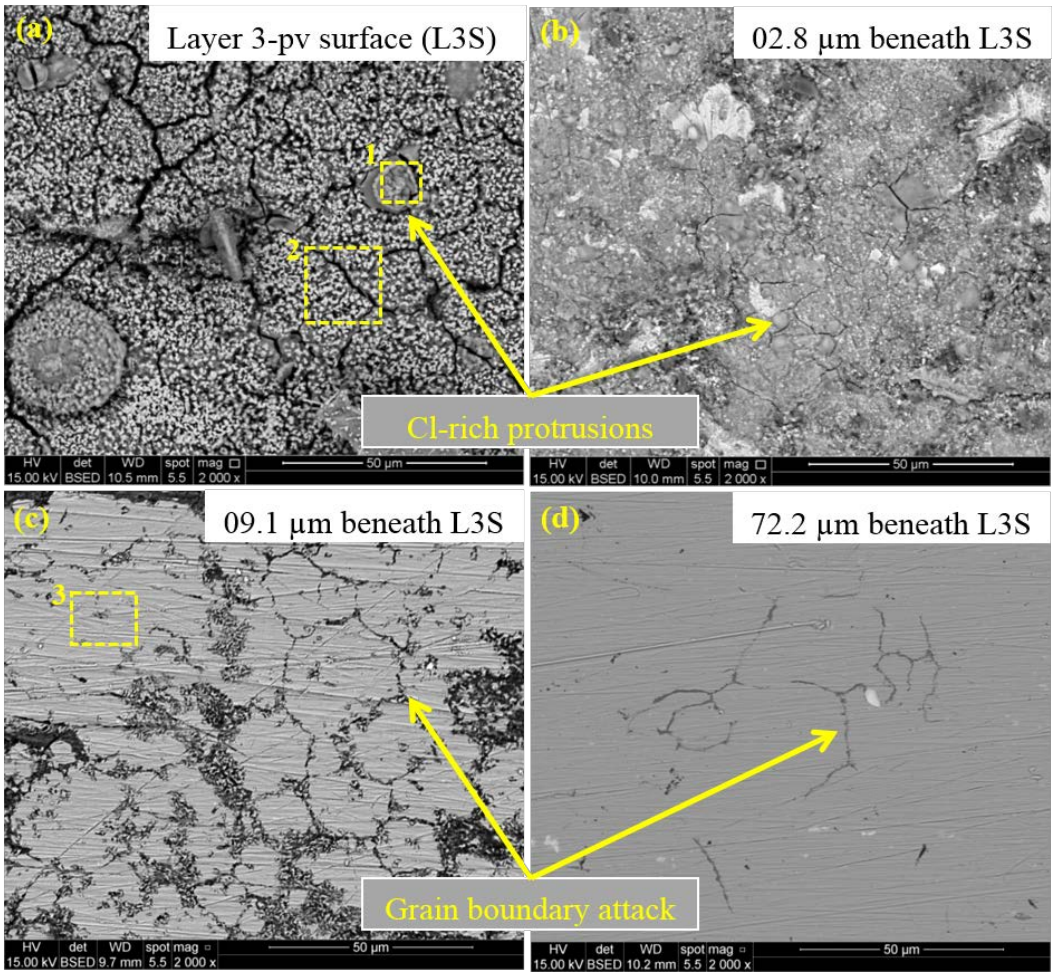

Figure 11. BSE micrographs showing microstructure changes of the internal corrosion regions revealed by successive removal of the porous layers starting from the original interface between layer 2-pv and layer 3-pv (Fig. 11a, i.e. point (vii) in Fig. 2). The associated depths shown in b)-d), have been estimated from the weight of the removed corrosion products and the densities of the prevalent phases identified by XRD measurements. EDS results of the marked regions are given in Table 6.

Table 6. Elemental composition of selected regions on layer 3-pv of the corrosion product (see Fig. 11), determined by EDS-analysis

Image	Region	Element (wt.-%)								
		O	S	Cl	K	Cr	Mn	Fe	Si	Ni
Figure 11a	1	13.2	2.8	13.5	1.0	2.6	1.0	22.5	-	43.3
	2	20.1	11.3	3.7	0.9	2.5	1.1	22.9	1.0	36.6
Figure 11c	3	1.6	-	-	-	18.2	2.1	65.0	0.5[a]	12.2

[a] The determined Si concentration could have been influence by residual Si from the grinding process.

Protrusions very rich in Cl (13.5 wt.-%) are observed locally on layer 3-pv (see Fig. 11a-b). Fe, Cr, Si and low amounts of K (≤ 1 wt-%) were also identified by EDS-analysis on this layer. Empirically, the amount of K observed is too low to chemically balance both Cl^- and SO_4^{2-} anions. Interestingly, relative to the concentration of other cations, and the concentration of Ni in the bulk alloy (cf. Tables 1 and 6), only Ni enrichment is observed within the protrusions (up to 40 wt-%). This observation suggests that the observed Cl is possibly, chemically associated with Ni. With further progress towards the bulk of the sample, the corrosion attack is seen to proceed through grain boundary attack (Figs. 11c-d). Metal oxides ($FeCr_2O_4$ and Fe_2O_3) are also identified by XRD on the surface and sub-surface regions of layer 3-pv (Fig. 12).

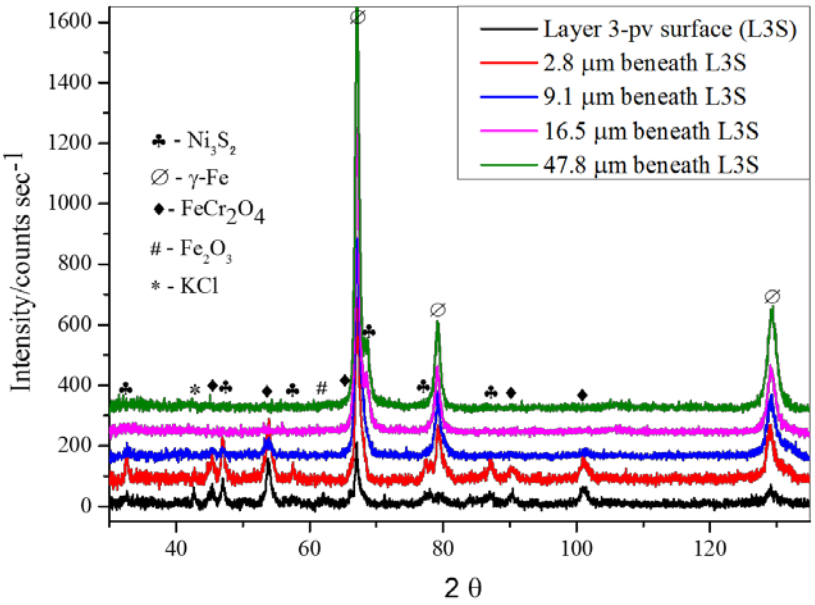

Figure 12. X-Ray diffractograms for various removals of layer 3-pv corresponding to the micrographs in Fig. 11.The associated depths have been estimated from the weight of the removed corrosion products and the densities of the prevalent phases identified by XRD.

However, the intensities of peaks from these phases are observed to decrease, as the bulk of the alloy is approached through removal of the corrosion product. Additionally, diffraction from nickel sulphide (Ni_3S_2) (JCPDS card 73-698) was recorded in the diffraction patterns as a function of distance from the surface of layer 3-pv. After an initial increase of the diffracted intensities of Ni_3S_2-peaks, they finally disappear as the bulk of the alloy is approached, which indicates that this phase is only located in a fairly thin region. Peaks from the γ-Fe phase, are seen to dominate with progress towards the bulk of the sample, indicating that the selective corrosion attack region becomes thinner during the course of the removal. No metal chloride phase could be identified from the XRD-measurements, probably because these phases exist only locally within the porous Ni-rich layer, as revealed by SEM (Figs. 11a-b).

In Fig. 13, a schematic summarizing the results from characterization of the corrosion product is shown. Results from both cross-sectional and plan view 'top-down' characterization methods showed that, the first layer (layer 1) was composed of partly molten KCl, segregates of K_2SO_4 and some Fe-oxide strands. Layer 2 was found to contain Fe_2O_3 and Fe_2CrO_4. In the selective attacked region (layer 3), Ni_3S_2 was identified. Metallic Cl-rich protrusions were also identified in this layer.

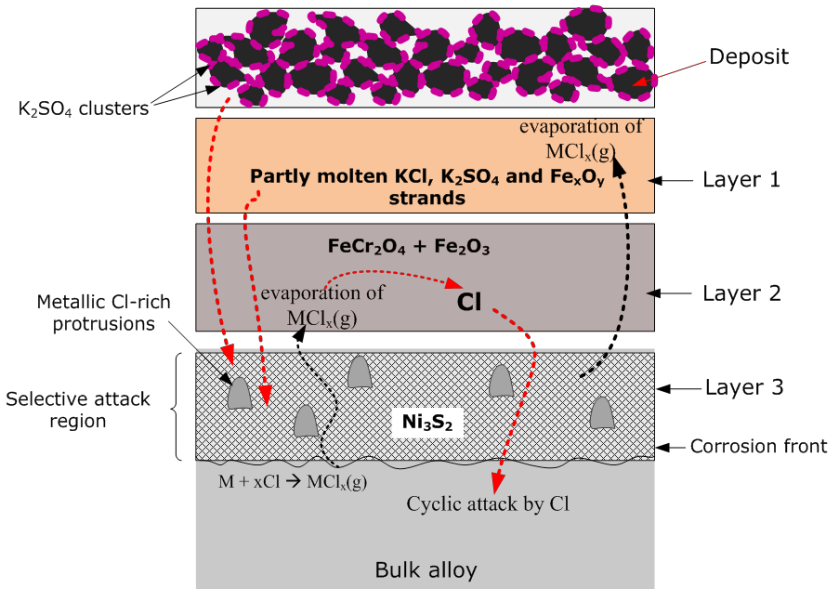

Figure 13. Schematic illustration of the prevalent corrosion products identified from both cross-sectional and plan view 'top-down' characterization methods.

3.3 Reaction product from the exposure of K_2CrO_4

Characterization of the reaction product arising from the exposure of K_2CrO_4 to straw-firing conditions revealed the formation of alkali metal sulphates. Characterization of the reaction products both by EDS-analysis and XRD showed the presence of K_2SO_4 in the reaction product

(see Fig 14 and Table 7). The observation of Na-containing phases in the diffractogram was due to Na impurities present in the as-received K_2CrO_4, as indicated in the specification sheet [37].

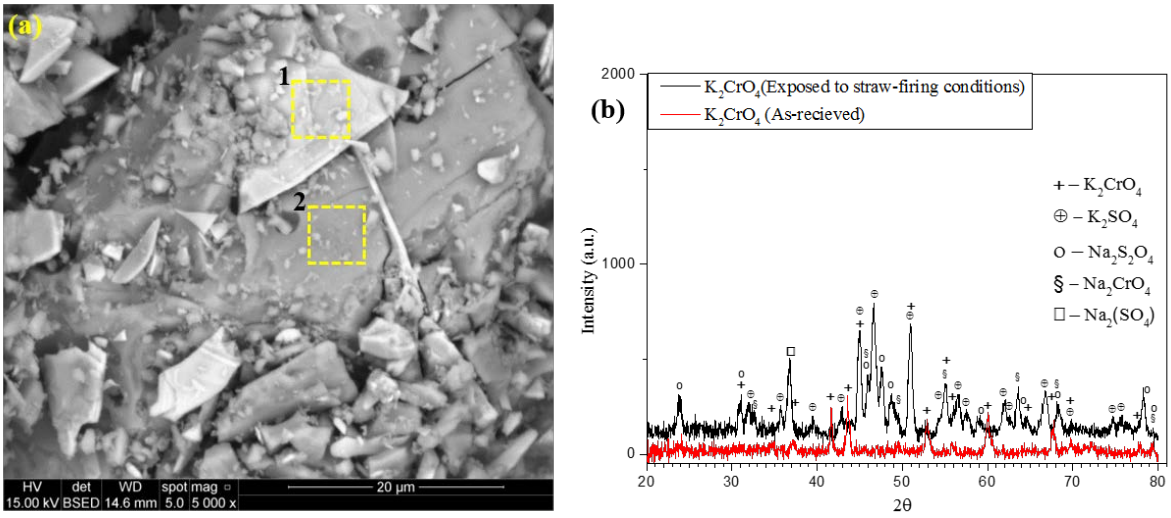

Figure 14. Exposure of K_2CrO_4 to straw-firing conditions: (a) BSE micrograph of the reaction product. The corresponding EDS-analysis is presented in Table 7. (b) X-Ray diffractogram.

Table 7. Elemental composition of selected regions on the corrosion product resulting from exposure of K_2CrO_4 to straw-firing conditions (cf. Fig. 15a), determined by EDS-analysis

Image	Region	Element (wt.-%)				
		O	S	K	Cr	Na
Figure 15a	1	33.3	15.9	29.9	17.4	3.8
	2	31.9	20.4	43.9	2.0	1.8

4. Discussion

High temperature corrosion observed on superheater tubes during biomass firing is widely accepted to be caused by KCl, which condenses on heat exchanger surfaces. The catastrophic corrosion observed is frequently explained by the active oxidation mechanism catalyzed by Cl [2,17,18,38]. Initiation and sustaining mechanisms for the corrosion process are still being discussed in literature [22,27,30,38,39]. For Cr-containing alloys under oxidizing conditions, the K-induced breakaway corrosion of the initial protective Cr_2O_3 layer has been reported as the initiation process (equation 1) [5,21,40].

$$Cr_2O_3(s) + 4KCl(s) + 2H_2O(g) + \frac{3}{2}O_2(g) \rightleftharpoons 2K_2CrO_4(s) + 4HCl(g) \qquad (1)$$

The above reaction depletes the alloy of Cr, and thus results in the formation of a non-protective iron-rich oxide layer according to equation 2.

$$(Cr_{1-x,}Fe_x)_2O_3(s) + 4KCl(s) + \frac{3}{2}O_2(g) + 2H_2O \longrightarrow xFe_2O_3(s) + 2(1-x)K_2CrO_4(s) + 4HCl(g) \qquad (2)$$

The HCl generated from this reaction is able dissociate under oxidizing conditions to give $Cl_2(g)$ (equation 3) [20,38,41], which migrates through the porous oxide (possibly through grain boundaries), to the metal bulk where it chlorinates the metal alloying elements, to generate metal chlorides.

$$2HCl(g) + \frac{1}{2}O_2(g) \rightleftharpoons Cl_2(g) + H_2O(g) \qquad (3)$$

$$M(s) + xCl \rightleftharpoons MCl_x(s) \qquad (4)$$

The diffusion of chlorine can also progress through an electrochemical route involving the reduction of Cl at the scale surface and the oxidation of the metal below the scale surface [22,27,30].

However, in atmospheres containing $SO_2(g)$ (similar to experimental conditions of the present work), the sulphation of KCl is possible (equation 5), and thus the initiation as well as the overall corrosion mechanism may be different. By means of the plan view 'top-down' characterization approach applied in the present work, it is observed that the initial synthetic deposit consisting of pure KCl(s), becomes sulphated both at the flue gas/deposit and at the 'initial' deposit/oxide interface, after exposure to an SO_2 containing flue gas (see Figs. 6 and 7).

$$2KCl(s) + SO_2(g) + \frac{1}{2}O_2(g) + H_2O \rightleftharpoons K_2SO_4(s) + 2HCl(g) \qquad (5)$$

Difference in the flue gas concentration at the deposit/flue gas and deposit/corrosion product interfaces, might be a reason for the greater sulphation of the deposit particles at the deposit/flue gas interface. The sulphation of KCl will proceed with the adsorption of SO_2 on the KCl particles, forming the SO_3 intermediate, according to a Langmuir adsorption model as proposed for NaCl sulphation [42,43]. The round-shaped cluster accumulations (identified to be K_2SO_4 particles), around the KCl particles observed in Fig. 6, suggest that the K_2SO_4 must have formed through an adsorption process and thus supports the above mechanism. In Figs. 6 and 7, KCl was also identified in addition to K_2SO_4, thereby suggesting an incomplete sulphation. Some experiments have reported incomplete sulphation of KCl particles exposed to simulated straw firing conditions

[32], or a reduced sulphation of smaller sized KCl particles due to low porosity of the deposit, which limits effective transport of the flue gas through the entire deposit [33]. Nevertheless, the sulphation of KCl will generate HCl (equation 5), which would also catalyze the rapid corrosion of the alloy, since such reaction has been reported to also favor the chlorination reaction (equation 4) [20].

Furthermore, it is possible that under straw-firing conditions, the resulting K_2CrO_4 from equation (1) formed during the early stages of the corrosion process, becomes converted to K_2SO_4 according to equation 6.

$$4K_2CrO_4(s) + 4SO_2(g) \rightleftharpoons 4K_2SO_4(s) + 2Cr_2O_4(s) + O_2(g) \qquad (6)$$

The above reaction could account for the absence of K_2CrO_4 often identified in reports in literature for similar austenitic stainless steels (see for example [16,23,44]), in the present corrosion products, despite the extensive characterization process employed. Although the Reaction 6 is thermodynamically favourable (ΔG = -683 kJ(T = 500 ^oC) and -617 kJ(T = 600 ^oC)) [45], it is still unknown if the initiation process under straw-firing conditions proceeds according to the route in equation (1) and (2), which results in K_2CrO_4-formation, or through the additional stage according to equation (6). To substantiate this, pure K_2CrO_4 crystals were exposed in the present work to similar conditions simulating straw-firing. Results from the characterization of the reaction products from such exposure highlighted the presence of K_2SO_4 in the reaction product (see Fig 14 and Table 7), thereby suggesting that the initiation stage of the corrosion process could proceed through the attack by KCl on the initially formed Cr_2O_3 and a subsequent transformation of the resulting K_2CrO_4 to the stable K_2SO_4, or directly through the sulphation of KCl.

Plan view investigations below the sulphated deposit showed a fused layer rich in K and Cl, containing strands rich in Fe. This was also observed together with round-shaped particle agglomerates rich in K and S. The morphologies of these structures show that they have been partly molten (Figs. 8c, 8d, 9b and 9c). However, both KCl and K_2SO_4 exhibit melting temperatures above 560 ^oC. A potential explanation for such melts at 560 ^oC could be the formation of a eutectic, since neither pure KCl, nor K_2SO_4 can melt in the temperature range considered in the present experiments. The ability of KCl to form low-melting eutectics with transition metal chlorides in the temperature range (200 – 500 ^oC) has been reported previously [17,39]. With the depletion of Cr in the oxide and subsurface regions, due to reaction with K, according to equation (1), Fe-chloride formation from the chlorination reaction in equation (4), becomes thermodynamically favourable, and thus the formation of a eutectic melt with KCl below 560 ^oC is possible. In a melt phase, the rate of sulphation is significantly enhanced and more Cl is generated, which is able to penetrate the porous oxide layer and induce further chlorination of alloying elements [32,33,46].

The resulting metal chlorides formed by the chlorination reaction (4) are stable at the (reducing) oxide/alloy interface, and thus possess high equilibrium vapor pressures [41]. Identification of

metal chlorides, on local points close to or at the corrosion front between layer 3 and the bulk alloy (Figs. 11a-b, 12) affirms the stability of these species at such reducing locations. This as well confirms the role of Cl in the active oxidation mechanism. Earlier work has also identified metal chlorides at the corrosion front [23,47–49]. However, depending on the vapor pressure of the metal chloride, these species are able to evaporate and become oxidized upon reaching regions with relatively high oxygen potentials, according to equation (8).

$$MCl_x(s) \rightleftharpoons MCl_x(g) \qquad (7)$$

$$yMCl_x(g) + \frac{z}{2}O_2(g) \rightleftharpoons M_yO_z(s) + yCl_x(g) \qquad (8)$$

Part of the released Cl from the oxidation is able to migrate back through the resulting porous oxide to the corrosion front where it reactivates the chlorination reaction. It is worth noting that the Cl-activity (and thus, the Gibbs free energy) required for the chlorination of metal alloying elements at the corrosion front depends on the alloying element [20,41,50]. Ni is known to require a higher Cl activity (compared to Fe and Cr) in order to form the corresponding Ni-chloride [51]. This difference in Cl-activity may explain the significant increase in Ni-concentration observed within layer 3 of the corrosion product (see Figs. 4, 11 and Table 6). The Ni-rich, sponge-like layer must thus have been formed due to selective chlorination and oxidation of Cr and Fe from such regions, consequently leaving the most stable species (Ni) behind as a skeleton.

Dissimilarities in oxygen partial pressure, for the metal chloride to metal oxide transformation in equation (8), as well as the volatility of the metal chlorides, will determine the hierarchical and morphological arrangement of the resulting oxide layers. $CrCl_2$ has been reported to possess lower vapor pressure than $FeCl_2$ [20,41], thus it is realistic to observe a Cr-rich oxide close to the bulk alloy, and a Fe-rich oxide close to the flue gas/corrosion product interface. Such differences in metal chloride vapor pressures would also explain the identification of Fe in the corrosion product layers located at regions with higher oxygen partial pressures (see Figs. 4, 8c, 9b and the tables therein). Thematically, the identification of 1 wt.-% of Si on the surface of layer 3-pv indicated the precipitation of Si-oxide at such locations with low oxygen partial pressure, because of the low oxygen partial pressure required for oxidation of Si-chloride [41]. The Mn band observed in the EDS maps in Fig 4 is located above the Cr band because of the higher oxygen partial pressured required for conversion of Mn-chloride to Mn-oxide. Both cross-sectional and plan view 'top-down' characterization of the corrosion products by EDS-analysis showed that the lower region of the oxide layer (layer 2) contains predominantly Cr. Fe rich particles were located mostly within the sulphated K_2SO_4 and KCl partly molten layer (layer 1-pv) on the top regions of layer 2-cs (and layer 2-pv), and even at the deposit/corrosion product interface, thereby confirming that higher oxygen partial pressures are required for the conversion of Fe-chloride. Despite the dependence of metal-chloride to metal-oxide conversion on oxygen partial pressure, XRD-diffraction results do not show the separate formation of the two metal (Fe and Cr) oxides. This could be because the Cr-oxide formed is too thin to be detected by XRD, despite the grazing incidence measurements

employed in the current study. On the other hand, it is possible that the similar rhombohedral crystal structures of Cr_2O_3 and Fe_2O_3 would facilitate the formation of the spinel [$FeCr_2O_4$], as identified by XRD phase analysis (Fig. 10).

Interestingly, the successive removal and characterization of the sponge-like layer, (layer 3) of the corrosion product, using both XRD and EDS have shown that S also exists together with Ni in this layer and can be attributed to the Ni_3S_2 phase as confirmed by XRD phase analysis. Identification of Ni_3S_2 in the corrosion product indicates that, apart from active oxidation of the alloy exposed to straw-firing conditions, sulphidation may be an attack mode on the non-reacted nickel. The Ni sulphidation is observed to also proceed within the region of selective corrosion along grain boundaries (see Fig 11). The identification of sulphidation induced attack in corrosion products resulting from coal firing, as well as co-firing of straw with coal has been reported [52], and the responsible mechanism for sulphidation attack on Ni has been discussed by several authors [53–56]. For direct reaction between S and the metal, it is a requirement for the equilibrium partial pressure of S to be higher than that of the dissociation of the resulting metal sulphide. Additionally, the stability region of the metal oxide should overlap with that of the S partial pressure. Under such conditions, S from the flue gas can diffuse through the porous corrosion product layers to form the metal sulphide below these layers. The presence of metal alloying elements with high affinity for oxide formation (such as Cr) will catalyze the sulphidation attack by enhancing the transfer of S via direct reaction of SO_2 with the oxide former [53,55]. Another possible mechanism will involve direct transport of molecular SO_2 through cracks and pores in the corrosion product layers (layer 1 and 2), to the sponge-like Ni rich layer of the corrosion product (layer 3). At such position, the oxygen potential is relatively low and thus presents a non-oxidizing atmosphere which would facilitate the sulphidation reaction [53]. Seiersten and Kofstad [54], suggested that the sulphidation of Ni might involve the $NiSO_4$ intermediate, which converts to the sulphide at lower temperatures. However, such mechanism is expected to result in the formation of NiO and Ni_3S_2 in a 4:1 ratio. The formed NiO from outward diffusion of Ni often leads to detachment of the scale. However, the Ni_3S_2 containing layer (layer 3) observed in the present study showed no signs of detachment (see Fig 3c), thus it is unlikely that the sulphidation attack reported here proceeded according to the mechanism involving the $NiSO_4$ intermediate.

In summary, the present results from both cross-sectional and the plan view 'top-down' characterization of corrosion products, resulting from laboratory scale experiments, indicate that both active oxidation and sulphidation corrosion mechanisms operate during straw-firing.

5. Conclusions

Corrosion products on an austenitic stainless steel (TP 347H FG) exposed to simulated straw-firing conditions under laboratory conditions have been investigated. Thorough characterization of the complete surface region of the exposed sample was achieved from both cross section analysis and a plan view analysis in combination with removal of the corrosion products. Complementary

results were revealed from microscopic (LOM, SEM), spectroscopic (EDS) and diffraction analysis (XRD) as a function of distance from the initial deposit surface.

In particular the depth-resolved (plan view 'top-down') characterization approach revealed interesting features such as the formation of a KCl melt layer below the initial deposit and the local formation of Cl-rich melts at the corrosion front which are not always visible from cross sections only.

The combination of both the way of characterization (cross section and plan view as a function of depth) and the various characterization methods (LOM, SEM, EDS, XRD) revealed unique results, which are used to further validate the corrosion mechanisms under straw-firing conditions.

Based on the present results it is suggested that the sulphation of KCl as well as the formation of a KCl-Fe-chloride melt within the sulphate could be responsible for the generation of Cl to sustain the active oxidation mechanism.

The morphology and chemistry of the corrosion products show that for an austenitic stainless steel, both Cr and Fe are easily attacked by Cl according to the active oxidation mechanism.

Ni is not readily attacked by Cl and is left as a sponge-like layer due to selective oxidation of Cr and Fe. However, sulphidation of this unreacted nickel can occur.

AUTHOR INFORMATION

Corresponding Author

* Phone: +45 50185680, Fax: +45 45936213, Email: sunoko@mek.dtu.dk, okorochukwudi@ymail.com

ACKNOWLEDGMENT

This work is part of the Danish Strategic Research Centre, Power Generation from Renewable Energy (GREEN). The authors acknowledge funding by the Danish council for Strategic Research.

REFERENCES

[1] L.L. Baxter, T.R. Miles, T.R.J. Miles, B.M. Jenkins, D.C. Dayton, T.A. Milne, R.W. Bryers, L.L. Oden, The Behavior of Inorganic Material in Biomass-Fired Power Boilers-Field and Laboratory Experiences: Volume II of Alkali Deposits Found in Biomass Power Plants, 1996.

[2] H.P. Nielsen, F.J. Frandsen, K. Dam-Johansen, L.L. Baxter, The implications of chlorine-associated corrosion on the operation of biomass-fired boilers, Prog. Energy Combust. Sci.

26 (2000) 283–298.
[3] S. V. Vassilev, D. Baxter, L.K. Andersen, C.G. Vassileva, An overview of the chemical composition of biomass, Fuel. 89 (2010) 913–933.
[4] J. Pettersson, J.-E. Svensson, L.-G. Johansson, KCl-Induced Corrosion of a 304-type Austenitic Stainless Steel in O2 and in O2 + H2O Environment: The Influence of Temperature, Oxid. Met. 72 (2009) 159–177.
[5] J. Pettersson, H. Asteman, J.-E. Svensson, L.-G. Johansson, KCl Induced Corrosion of a 304-type Austenitic Stainless Steel at 600°C; The Role of Potassium, Oxid. Met. 64 (2005) 23–41.
[6] J.M. Johansen, J.G. Jakobsen, F.J. Frandsen, P. Glarborg, Release of K, Cl, and S during Pyrolysis and Combustion of High-Chlorine Biomass, Energy & Fuels. 25 (2011) 4961–4971.
[7] J.N. Knudsen, P.A. Jensen, K. Dam-Johansen, Transformation and Release to the Gas Phase of Cl, K, and S during Combustion of Annual Biomass, Energy & Fuels. 18 (2004) 1385–1399.
[8] J.N. Knudsen, P.A. Jensen, W. Lin, F.J. Frandsen, K. Dam-Johansen, Sulfur Transformations during Thermal Conversion of Herbaceous Biomass, Energy & Fuels. 18 (2004) 810–819.
[9] P.A. Tchoffor, K.O. Davidsson, H. Thunman, Transformation and Release of Potassium, Chlorine, and Sulfur from Wheat Straw under Conditions Relevant to Dual Fluidized Bed Gasification, Energy & Fuels. 27 (2013) 7510–7520.
[10] M.S. Bashir, P.A. Jensen, F. Frandsen, S. Wedel, K. Dam-Johansen, J. Wadenbäck, S.T. Pedersen, Ash transformation and deposit build-up during biomass suspension and grate firing: Full-scale experimental studies, Fuel Process. Technol. 97 (2012) 93–106.
[11] M.S. Bashir, P.A. Jensen, F. Frandsen, S. Wedel, K. Dam-Johansen, J. Wadenbäck, S.T. Pedersen, Suspension-Firing of Biomass. Part 1: Full-Scale Measurements of Ash Deposit Build-up, Energy & Fuels. 26 (2012) 2317–2330.
[12] M.S. Bashir, P.A. Jensen, F. Frandsen, S. Wedel, K. Dam-Johansen, J. Wadenbäck, Suspension-Firing of Biomass. Part 2: Boiler Measurements of Ash Deposit Shedding, Energy & Fuels. 26 (2012) 5241–5255.
[13] F.J. Frandsen, Ash Formation, Deposition and Corrosion when Utilizing Straw for Heat and Power Production, Dr. Techn. Thesis, Department of Chemical and Biochemical Engineering, Technical Univeristy of Denmark. ISBN: 9788792481405, Kongens Lyngby, 2011.
[14] K.A. Christensen, H. Livbjerg, A Field Study of Submicron Particles from the Combustion of Straw, Aerosol Sci. Technol. 25 (1996) 185–199.
[15] K.A. Christensen, M. Stenholm, H. Livbjerg, The formation of submicron aerosol particles, HCl and SO2 in straw-fired boilers, J. Aerosol Sci. 29 (1998) 421–444.
[16] P.A. Jensen, M. Stenholm, P. Hald, Deposition Investigation in Straw-Fired Boilers, Energy & Fuels. 11 (1997) 1048–1055.
[17] H.P. Michelsen, F.J. Frandsen, K. Dam-Johansen, O.H. Larsen, Deposition and high temperature corrosion in a 10 MW straw fired boiler, Fuel Process. Technol. 54 (1998) 95–108.
[18] M. Montgomery, A. Karlsson, In-situ corrosion investigation at Masnedø CHP plant - a straw-fired power plant, Mater. Corros. 50 (1999) 579–584.
[19] M. Montgomery, A. Hansson, O. Biede, T. Vilhelmsen, High temperature Corrosion testing

at Maribo Sakskøbing Biomass Firing Power Plant, in: J. Lecomte-Beckers, Q. Contrepois, T. Beck, B. Kuhn (Eds.), 9th Liege Conf. Mater. Adv. Power Eng., 2010: pp. 1096–1105.
[20] M. Montgomery, A. Karlsson, O.H. Larsen, Field test corrosion experiments in Denmark with biomass fuels. Part 1: Straw-firing, Mater. Corros. 53 (2002) 121–131.
[21] J. Pettersson, J.E. Svensson, L.G. Johansson, Alkali Induced Corrosion of 304-Type Austenitic Stainless Steel at 600°C; Comparison between KCl, K2CO3 and K2SO4, Mater. Sci. Forum. 595-598 (2008) 367–375.
[22] N. Folkeson, T. Jonsson, M. Halvarsson, L.-G. Johansson, J.-E. Svensson, The influence of small amounts of KCl(s) on the high temperature corrosion of a Fe-2.25Cr-1Mo steel at 400 and 500°C, Mater. Corros. 62 (2011) 606–615.
[23] Y.S. Li, M. Spiegel, S. Shimada, Corrosion behaviour of various model alloys with NaCl–KCl coating, Mater. Chem. Phys. 93 (2005) 217–223.
[24] S. Enestam, D. Bankiewicz, J. Tuiremo, K. Mäkelä, M. Hupa, Are NaCl and KCl equally corrosive on superheater materials of steam boilers?, Fuel. 104 (2013) 294–306.
[25] S. Karlsson, J. Pettersson, L.-G. Johansson, J.-E. Svensson, Alkali Induced High Temperature Corrosion of Stainless Steel: The Influence of NaCl, KCl and CaCl2, Oxid. Met. 78 (2012) 83–102.
[26] J. Lehmusto, B.-J. Skrifvars, P. Yrjas, M. Hupa, High temperature oxidation of metallic chromium exposed to eight different metal chlorides, Corros. Sci. 53 (2011) 3315–3323.
[27] N. Folkeson, L.-G. Johansson, J.-E. Svensson, Initial Stages of the HCl-Induced High-Temperature Corrosion of Alloy 310, J. Electrochem. Soc. 154 (2007) C515.
[28] H. Asteman, M. Spiegel, Investigation of the HCl (g) attack on pre-oxidized pure Fe, Cr, Ni and commercial 304 steel at 400°C, Corros. Sci. 49 (2007) 3626–3637.
[29] C. Pettersson, J. Pettersson, H. Asteman, J.-E. Svensson, L.-G. Johansson, KCl-induced high temperature corrosion of the austenitic Fe–Cr–Ni alloys 304L and Sanicro 28 at 600°C, Corros. Sci. 48 (2006) 1368–1378.
[30] T. Jonsson, N. Folkeson, J.-E. Svensson, L.-G. Johansson, M. Halvarsson, An ESEM in situ investigation of initial stages of the KCl induced high temperature corrosion of a Fe–2.25Cr–1Mo steel at 400°C, Corros. Sci. 53 (2011) 2233–2246.
[31] S. Sroda, S. Tuurna, Laboratory scale tests on corrosion behavior of boiler materials in simulated combustion atmospheres (EU Project – OPTICORR), Mater. Corros. 57 (2006) 244–251.
[32] H.P. Nielsen, F.J. Frandsen, K. Dam-Johansen, Lab-Scale Investigations of High-Temperature Corrosion Phenomena in Straw-Fired Boilers, Energy & Fuels. 13 (1999) 1114–1121.
[33] S.C. Van Lith, F.J. Frandsen, M. Montgomery, T. Vilhelmsen, S.A. Jensen, Lab-scale Investigation of Deposit-induced Chlorine Corrosion of Superheater Materials under Simulated Biomass-firing Conditions. Part 1: Exposure at 560 °C, Energy & Fuels. 59 (2009) 3457–3468.
[34] K.E. Coleman, N.J. Simms, P.J. Kilgallon, J.E. Oakey, Corrosion in Biomass Combustion Systems, Mater. Sci. Forum. 595-598 (2008) 377–386.
[35] H.J. Grabke, D.B. Meadowcroft, eds., A Working Party Report on Guidelines for Methods of Testing and Research in High Temperature Corrosion, European Federation of Corrosion Publications, 1995.
[36] K. Pantleon, M. Montgomery, Phase Identification and Internal Stress Analysis of Steamside Oxides on Plant Exposed Superheater Tubes, Metall. Mater. Trans. A. 43A

(2012) 1477–1486.
[37] Sigma-aldrich, K2CrO4 Product Specification, (2014). http://www.sigmaaldrich.com/catalog/product/sial/216615?lang=en&region=DK.
[38] R.A. Antunes, M.C.L. de Oliveira, Corrosion in biomass combustion: A materials selection analysis and its interaction with corrosion mechanisms and mitigation strategies, Corros. Sci. 76 (2013) 6–26.
[39] S.C. Cha, M. Spiegel, Local reactions of KCl particles with iron, nickel and chromium surfaces, Mater. Corros. 57 (2006) 159–164.
[40] J. Lehmusto, B.-J. Skrifvars, P. Yrjas, M. Hupa, Comparison of potassium chloride and potassium carbonate with respect to their tendency to cause high temperature corrosion of stainless 304L steel, Fuel Process. Technol. 105 (2013) 98–105.
[41] A. Zahs, M. Spiegel, H. Grabke, The influence of alloying elements on the chlorine-induced high temperature corrosion of Fe-Cr alloys in oxidizing atmospheres, Mater. Corros. 50 (1999) 561–578.
[42] L. Boonsongsup, K. Iisa, W.J. Frederick, Kinetics of the Sulfation of NaCl at Combustion Conditions, Ind. Eng. Chem. Res. 5885 (1997) 4212–4216.
[43] K. Iisa, Y. Lu, K. Salmenoja, Sulfation of Potassium Chloride at Combustion Conditions, Energy & Fuels. 13 (1999) 1184–1190.
[44] J. Lehmusto, P. Yrjas, B.-J. Skrifvars, M. Hupa, High temperature corrosion of superheater steels by KCl and K2CO3 under dry and wet conditions, Fuel Process. Technol. 104 (2012) 253–264.
[45] A. Roine, HSC Chemistry Ver 7, (2009).
[46] L.A. Hansen, H.P. Nielsen, F.J. Frandsen, K. Dam-Johansen, S. Hørlyck, A. Karlsson, Influence of deposit formation on corrosion at a straw-fired boiler, Fuel Process. Technol. 64 (2000) 189–209.
[47] P. Viklund, A. Hjörnhede, P. Henderson, A. Stålenheim, R. Pettersson, Corrosion of superheater materials in a waste-to-energy plant, Fuel Process. Technol. 105 (2013) 106–112.
[48] K. Salmonoja, M. Hupa, R. Backman, Laboratory studies on the influence of gaseous HCl on fireside corrosion of superheaters, J. Inst. Energy. 72 (1999) 127–133.
[49] H.J. Grabke, E. Reese, M. Spiegel, The effects of chlorides, hydrogen chloride, and sulfur dioxide in the oxidation of steels below deposits, Corros. Sci. 37 (1995) 1023–1043.
[50] M. Spiegel, A. Zahs, H.J. Grabke, Fundamental aspects of chlorine induced corrosion in power plants, Mater. High Temp. 20 (2003) 153–159.
[51] R. Bender, M. Schütze, The role of alloying elements in commercial alloys for corrosion resistance in oxidizing-chloridizing atmospheres part I: Literature evaluation and thermodynamic calculations on phase stabilities, Mater. Corros. 54 (2003) 567–586.
[52] M. Montgomery, O.H. Larsen, Field test corrosion experiments in Denmark with biomass fuels. Part 2: Co-firing of straw and coal, Mater. Corros. 53 (2002) 185–194.
[53] W.J. Quadakkers, A.S. Khanna, H. Schuster, H. Nickel, Investigation of the corrosion mechanisms of nickel and nickel-based alloys in SO2-containing environments using an evolved gas analysis technique, Mater. Sci. Eng. A. 120-121 (1989) 117–122.
[54] M. Seiersten, P. Kofstad, The high temperature corrosion of nickel in SO2 at 500–800°C, Corros. Sci. 22 (1982) 487–506.
[55] N.N. Aung, X. Liu, Effect of SO2 in flue gas on coal ash hot corrosion of Inconel 740 alloy – A high temperature electrochemical sensor study, Corros. Sci. 76 (2013) 390–402.

[56] N.N. Aung, X. Liu, Effect of temperature on coal ash hot corrosion resistance of Inconel 740 superalloy, Corros. Sci. 82 (2014) 227–238.